



OPEN

Asymmetric pathways in the electrochemical conversion reaction of NiO as battery electrode with high storage capacity

Ulrike Boesenberg^{1,2}, Matthew A. Marcus³, Alpesh K. Shukla¹, Tanghong Yi⁴, Eamon McDermott^{5*}, Pei Fen Teh^{1,6}, Madhavi Srinivasan⁶, Alexander Moewes⁵ & Jordi Cabana^{1,4}

¹Environmental Energy Technologies Division, Lawrence Berkeley National Laboratory, Berkeley, CA 94720, USA, ²Deutsches Elektronen-Synchrotron DESY, Notkestr. 85, D-22607 Hamburg, Germany, ³Advanced Light Source, Lawrence Berkeley National Laboratory, Berkeley, CA 94720, USA, ⁴Department of Chemistry, University of Illinois at Chicago, Chicago, IL 60607, USA, ⁵Department of Physics and Engineering Physics, University of Saskatchewan, Saskatoon, SK, Canada, ⁶School of Materials Science and Engineering, Nanyang Technological University, Singapore.

Electrochemical conversion reactions of transition metal compounds create opportunities for large energy storage capabilities exceeding modern Li-ion batteries. However, for practical electrodes to be envisaged, a detailed understanding of their mechanisms is needed, especially vis-à-vis the voltage hysteresis observed between reduction and oxidation. Here, we present such insight at scales from local atomic arrangements to whole electrodes. NiO was chosen as a simple model system. The most important finding is that the voltage hysteresis has its origin in the differing chemical pathways during reduction and oxidation. This asymmetry is enabled by the presence of small metallic clusters and, thus, is likely to apply to other transition metal oxide systems. The presence of nanoparticles also influences the electrochemical activity of the electrolyte and its degradation products and can create differences in transport properties within an electrode, resulting in localized reactions around converted domains that lead to compositional inhomogeneities at the microscale.

The use of electrochemistry to harvest the energy of chemical bonds was first proposed in the 18th century¹, but has recently experienced an intense boost of interest as part of the efforts to reduce our dependence on fossil fuels. The amount of energy is proportional to the number of electrons involved in the redox reaction, but so is the extent of atomic rearrangement, which creates kinetic barriers that decrease the energy efficiency of the process. Batteries add one further fundamental challenge: besides redox flow cells², the technologies considered today involve compounds in the solid state³. While this approach maximizes energy density, it imposes new penalties, in the form of sluggish transport and mechanical energy. Indeed, the redox reactions that lead to the highest storage capacity also involve the most colossal volume changes^{4,5}, changes of fundamental transport properties, enhanced reactivity, and even transitions across states of matter⁶. In practice, commercial devices sacrifice energy density for the sake of power density and durability⁷. Given that these devices fall short of the requirements in applications such as transportation, the race continues to devise inventive means to break the existing barriers.

With the goal of maximizing energy storage, exploiting the reversible conversion of transition metal based compounds, M_aX_b ($X = N, O, F, P, S, H$), to metal nanoparticles and Li_nX salts becomes tempting⁵. The reactivity is generalized across the Periodic Table, meaning that low cost and toxicity compounds can be proposed. Further, the cell voltage is tunable depending on the selected ions⁵. Interestingly, extremely small and defective nanoparticles are preserved during the reaction⁸, a feature that is attractive when new routes to the production of catalysts are sought⁹. Despite their apparent simplicity, application of electrochemical conversion reactions in batteries is limited by chemical inefficiencies. The reactions take place in the solid state and involve mass transport of species in addition to Li^+ , creating diffusional bottlenecks^{8,10} and resulting in enormous shape changes, which eventually lead to premature failure through particle disconnection. Further, while formation of nanoscale particles with large surface areas is beneficial in terms of reactivity and mass transport, the large surfaces also

SUBJECT AREAS:
MATERIALS CHEMISTRY
MATERIALS FOR ENERGY AND
CATALYSIS

Received
4 September 2014

Accepted
4 November 2014

Published
20 November 2014

Correspondence and
requests for materials
should be addressed to
J.C. (jcabana@uic.
edu)

* Current address:
Institute of Materials
Chemistry, TU Wien,
A-1060 Vienna,
Austria.



promote undesired side reactions with the electrolyte¹¹. The result is a gel-like layer of inorganic and organic compounds around the particles¹². Since charge *and* mass need to be transported through this layer, its reactivity, conductivity and structural properties are yet another kinetic bottleneck.

Perhaps the most important barrier to application of conversion reactions is the huge voltage hysteresis between the reduction (conversion) and oxidation (deconversion) reaction⁵, which significantly lowers the roundtrip energy efficiency of the device. In the initial cycle, a portion of this hysteresis was ascribed to the surface penalty imposed by the formation of nanocrystalline metal particles^{10,13}. Accordingly, hysteresis gets smaller on subsequent cycles, once irreversible microstructural changes have occurred⁵, but remains excessively high. It has also been proposed that the need for diffusion of multiple species imposes different pathways, involving different intermediates, for the reduction (conversion) and oxidation (deconversion) steps. This hypothesis was validated with FeF₃, where minimizing the need for Feⁿ⁺ ions to move was predicted to lead to Li_xFeF₃ and a collection of Li-Fe³⁺-F compounds as the favored intermediates on reduction and oxidation, respectively. Hysteretic pathways, involving different intermediates, were also experimentally observed for Mn₃O₄¹⁴. However, in the case of a much simpler phase diagram, such as that of Li-Bi-F, the voltage hysteresis could not be explained by intermediate or ternary phases¹⁵. It suggests that a fundamental driving force for hysteresis exists and is common to all systems. Interestingly, in general, studies of the reaction mechanism using short range probes typically report that the conversion largely reverses back directly to the initial chemical state, especially in binary compounds with metals in low oxidation states^{16–18}.

Here, we aim to present a complete picture over multiple length scales of electrochemical conversions with lithium, tying mechanisms at different length scales so as to define their specific origins and possible intertwining. NiO was chosen as a model system for the simplicity of the Li-Ni-O phase diagram¹⁹, which, in principle, creates few possibilities for alternative pathways. In other words, involvement of intermediate redox couples between Ni²⁺ and Ni⁰ on reduction and oxidation, as reported for FeF₃ and Mn₃O₄, among others, is not expected. Yet electrochemical hysteresis has recently been linked to thermodynamic effects¹³. The study employs X-ray absorption spectroscopy (XAS) in different conditions such as energy, electrochemical coupling and spot size. XAS probes the electronic structure in the immediate vicinity of an atom while averaging over a large sample volume without limitations to structural properties and, thus, bears an advantage over diffraction for the study of conversion reactions, as the amorphous or nanoscale phases that commonly form cannot be resolved by XRD²⁰. The formation of metallic nanoclusters was found to be central to all observations.

Results

Chemical output during electrochemical conversion reaction.

Figure 1 shows the first galvanostatic cycle of the Li metal cell containing bulk NiO (NiO-B) used for *operando* XAS at the Ni K edge, as well as the results from principal component analysis (PCA) of the XAS data. Iterative target-factor analysis (ITFA) was used to extract the number of components present in the system²¹. In this particular case, they were found to directly correspond to chemical phases, so the figure also shows the correlation between the electrochemical behavior and evolution of the phase fractions. A detailed discussion will be provided below. Electrochemical data for electrodes in conventional coin cells was largely comparable (figure S1 in the Supplementary Information), although the length of the sloping region was found to be shorter than in the *operando* cell. The small discrepancy in capacity may be due to enhanced electrolyte side reactions (see below) in the large volume pouch cell used for the *operando* measurement. The initial reduction process at 0.8 V is likely to be related to side reactions, possibly solvent

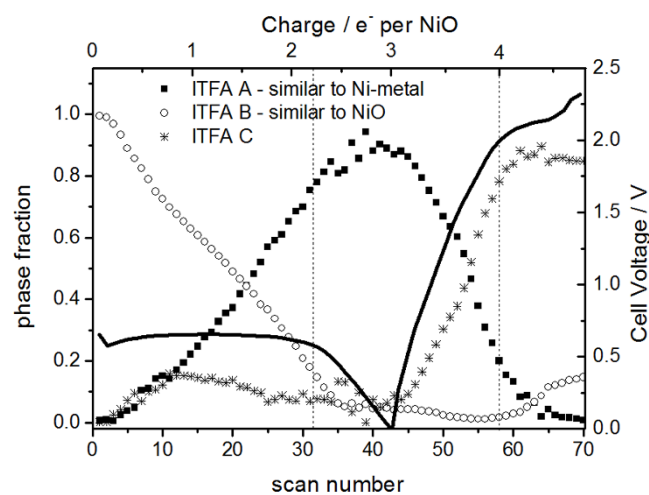


Figure 1 | Electrochemical profile (black line) of a two-electrode cell containing NiO-B as working and lithium metal as counter and pseudo-reference electrodes designed for simultaneous collection of Ni K-edge XAS data. The cell was galvanostatically cycled at a C/7.5 rate. Phase fractions obtained from principal component analysis of the XAS data are indicated symbols (ITFA A – full squares, ITFA B – open circles, ITFA C – stars). The bottom abscissa is the XANES scan number; the upper abscissa is the corresponding number of electrons transferred per NiO. The vertical lines after 2.2 transferred e⁻ (scan 32) and 4 e⁻ (scan 58) indicate the end of the two phase plateau during reduction and the beginning of the pseudo-plateau during oxidation.

reduction^{12,14}. The long plateau at 0.65 V corresponds to the conversion reaction of NiO to Li₂O and metallic Ni. This plateau was followed by an extended slope, with an overall specific capacity exceeding the theoretical value for the reduction of the oxide, 718 mAh/g (or 2 mol electrons/mol NiO). The capacity during the sloping region was largely reversibly upon oxidation, followed by a single pseudoplateau at approximately 2.1 V. It is apparent that a significant portion of the charge invested in the reduction reaction is not recovered upon oxidation, resulting in a large coulombic inefficiency. Comparison of the voltage values at which plateaus developed on reduction and oxidation revealed a voltage hysteresis of 1.4 V. Combined with the large coulombic inefficiency, the result is the unacceptably large roundtrip inefficiency common to conversion electrodes.

Figure 2a displays the X-ray absorption near edge structure (XANES) region of spectra for selected points collected during reduction under *operando* conditions. The spectrum of pristine NiO showed a steep edge and high white-line at approximately 8350 eV. As the reaction proceeded, the absorption edge increased in spectral weight at lower energies and the white-line decreased, a typical spectral feature of a metallic phase. The well-known formation of nanoparticles⁵ explains the weakening of the post-edge features above 8350 eV. The aligning isosbestic points (inset in figure 2a) support the assumption of a two-phase reaction, but given their sensitivity to spectral correction, this observation can only be taken as a first indication.

Principal component analysis (PCA) was performed for the whole collection of spectra to estimate the number of independently-varying components. Note that each PCA component may consist of multiple species, but in constant proportions. Iterative target factor analysis (ITFA) was used to recombine the abstract components into plausible “end-members” (ITFA components in Figure 2b). These components were then used in linear combination (LC) fits of all the spectra in order to quantitatively relate composition with the macroscopic electrochemical signatures. The results are also summarized in Figure 1. PCA indicated the presence of at least three unique

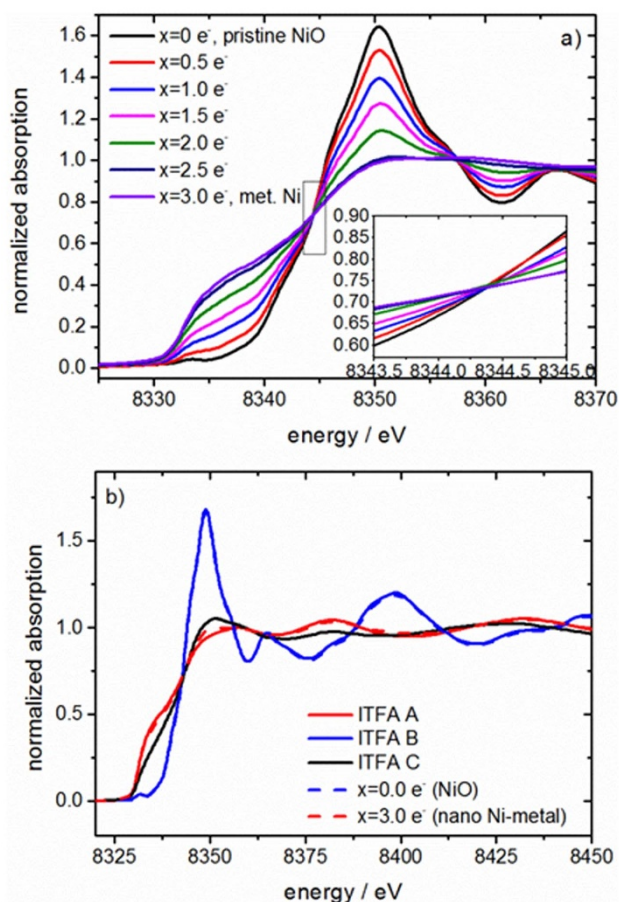


Figure 2 | (a) Ni K-edge XANES of discharge reaction at selected points during *operando* measurements of NiO-B; (b) XANES region of the determined ITFAs, overlaid with traces corresponding to NiO and nanoscale Ni.

components A, B and C, which could not be described as a linear combination of each other. Figure S2a in the Supplementary Information plots the first 4 abstract components, where the 4th component is only related to noise/background. Figure S2b and c in the Supplementary Information discuss the improvement of the fit of 4 vs. 3 vs. 2 components for selected scans (almost fully reduced and approximately $3.8e^-$ transferred). The existence of three components explains the imperfect isosbestic points. While PCA was performed in energy space over the full spectra, only the XANES region is displayed in figure 2b. It is important to note that, in general, one ITFA component does not necessarily correspond to an individual chemical phase. However, in the present case, components A and B were found to be highly similar to finely divided Ni and NiO, respectively (Figure 2b). On the contrary, component C could not be fully identified. Compared with component A, it presented a discernibly sharper white-line with the edge slightly shifted towards higher energies (i.e., slightly oxidized Ni). Further, the post-edge peaks were even less distinct than in nanometric Ni (ITFA A), indicating the defective and very short range coherence of this component. Its nature will be discussed in more detail below.

As expected, the phase fraction of ITFA component A increased at the expense of B, corresponding to the conversion of NiO to metallic Ni. Besides these two components, PCA revealed the minor but distinct presence of ITFA component C throughout the discharge reaction. The existence of this third component is a deviation from the two phase picture typically presented in conversion reactions. The conversion of NiO to metallic Ni was not complete at the end of the plateau (see dashed line), but continued in the following sloping

region. During this tail-end of the reaction, approximately 5–10% of NiO was converted while about 20% of the total charge was transferred. This indicates two issues. First, a fraction of the active material requires a greater overpotential for conversion to occur, which might be due to partial loss of electrical contact due to mechanical damage and/or surface reactions. Second, a significant amount of the electrons transferred between electrodes in the cell participate in side reactions, both during the plateau as well as during the sloping tail. As a result, the fact that the number of electrons measured during the voltage plateau largely matches the stoichiometric ratio in the conversion reaction can be considered (Figure S1 in the Supplementary Information), to some extent, arbitrary, and not a true measure of the efficiency of the reaction.

Comparison between the Li K-edge XAS data of NiO electrodes at different points of the reaction with pure compounds such as LiF, Li₂CO₃, Li₂O and LiOH (Figure 3), known components of electrolyte reaction layers²², revealed that these reactions significantly contributed to the extra capacity²³. The data were sensitive to probing depths of approximately 20–50 nm²⁴, i.e., to the sample surface exclusively. The most prominent signatures at all states were assigned to LiF, even when the electrode was only partly reduced, thus confirming that electrolyte decomposition occurred during the conversion plateau. No significant signals of Li₂O were detected even after one full reduction. Complementary TEM analysis of NiO nanoparticles (NiO-NP) particles at the end of the conversion plateau revealed a coating of a few nm thickness (Figure S3 in the Supplementary Information), where EELS, which is sensitive to the bulk of the sample, confirmed the formation of Li₂O and its reversible consumption to produce a NiO-like compound (Figure S4 in the Supplementary Information). Over the course of the reaction, the composition of the layer was dynamic, with a contribution of Li₂CO₃ to the Li K edge XAS becoming apparent upon oxidation.

Structural implications of the electrochemical conversion. A quantitative model using the peak intensity of the first shell was employed to fit the EXAFS data from the *operando* experiment. Under the assumption of constant and theoretical coordination numbers, the passive electron reduction factor, S_0^2 , was fitted as a magnitude of the total scattering amplitude for pristine NiO-B, which was then used as a constant for the consecutive scans on the PCs. Apparent coordination numbers (CN) were obtained in these cases. The obtained CN are a convolution of coordination number, changes in S_0^2 due to the chemical reaction and bond-length

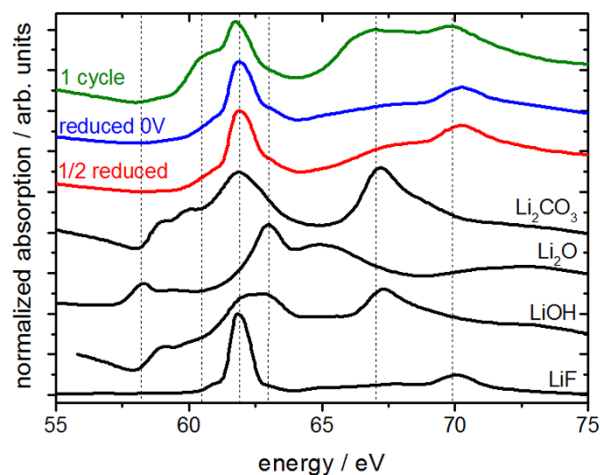


Figure 3 | Soft XAS at the Li K-edge for NiO electrodes in various stage of charge/discharge (top) as well as reference compounds (bottom). This data was collected in total fluorescence yield from at the top of the electrodes.



distribution; they can therefore not be taken as absolute value of coordination. Some fits after and during reduction showed extremely small apparent CN both for Ni-Ni and Ni-O, which would be prohibited by the conservation of local charge balance. Fitting was performed only up to a radius of 3 Å including the first Ni-Ni shell for all data because of i) evident loss of long range order during the reaction and ii) to avoid inaccuracy due to many multiple scattering paths with large relative amplitude²⁵. Figure 4 shows the magnitudes of the Fourier transform for selected scans during the discharge reaction (solid trace) and the corresponding fit (dashed line). The resulting fitting parameters and quality of the fit are summarized in Table 1. A complete list of all parameters and fit results can be found in Table S1 in the Supplementary Information.

The pristine material showed a first shell corresponding to Ni-O bonds with a distance of approximately 2.08 Å, the second shell corresponding to Ni-Ni bonds at 2.95 Å. These distances match bulk NiO²⁶. Peaks ascribed to higher coordination shells were well resolved, indicative of the long range order in the material. During the reduction (scans 1–42), the intensity of the Ni-O and Ni-Ni peaks of NiO decreased and a new peak appeared at approximately 2.5 Å, corresponding to the Ni-Ni bond in Ni. This feature dominated the spectra from approx. 1.5 e⁻ transferred (scan 21) onwards, indicative of a steady conversion. In the fully reduced state, at 0 V, only this Ni-Ni shell in metallic Ni contributed to the EXAFS signal. Scattering from higher shells was almost undetectable; long range order was lost during the first reduction, consistent with the formation of very small metallic domains. No particle growth of the newly formed Ni particles seemed to take place, since no peaks from higher coordination shells appeared, in good agreement with observations in other conversion systems^{8,27}. The Ni-Ni bond length of the fully reduced sample was slightly contracted compared to bulk Ni, as it is typical for nanoparticles^{27,28}. The spectral intensity amplitude was reduced to almost half the initial value in the course of the *operando* measurements, which was accounted for by a reduced apparent coordination number (CN), under the assumption of constant S₀². Theory predicts an intensity reduction by about 13% for particles with a diameter of about 3 nm due to so called termination effects²⁹. Recent experimental work showed much larger intensity reductions up to 41%³⁰, which were explained by substitution of phosphorus into the nickel lattice. Another factor for the obtained value for the CN is also the bond length distribution. Thus, the large intensity reduction in the present case is possibly caused by the large number of defects and disorder present in the formed Ni particles.

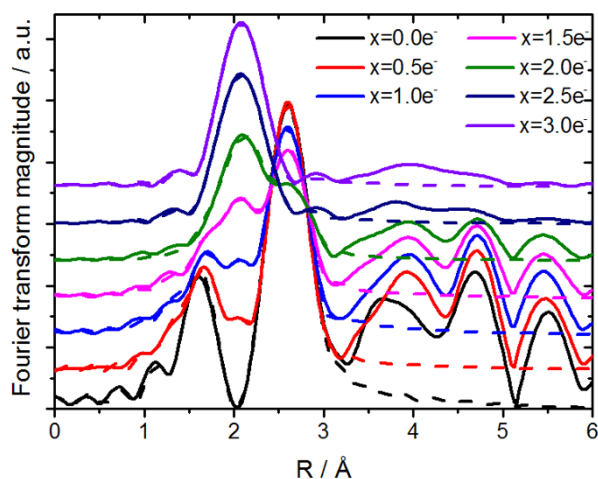


Figure 4 | Fourier transform magnitude of k^3 weighted Ni-K-edge EXAFS spectra (solid line) and the corresponding fit (dashed line) of NiO-B and at selected points during the reduction in a Li metal cell, taken from *operando* measurements.

Little is known about the implications at the microscopic scale of domains of highly conductive metal forming in a matrix of semiconducting material. NiO-B electrodes were reduced to a formal 50% conversion, at two different rates to be measured *ex-situ*. Ni chemical maps at 5 μm resolution of significant electrode portions were obtained by μ-XAS mapping using a TFY detector (Figure 5). The data corresponds to volumes of a few microns into the face of the electrode exposed to the electrolyte in the coin cell geometry, the current collector being on the opposite end. Micron-scale lateral inhomogeneities were apparent in the electrode reduced slowly, and became strikingly more severe when the reaction was performed at a faster rate, producing Ni (red) and NiO (blue) domains of hundreds of microns. Comparison between spectra at discrete points in the map with data simultaneously collected with a surface-sensitive (5–10 nm) TEY detector (Figure S5 in the Supplementary Information), revealed additional in-depth chemical gradients: a tendency was found towards higher metallic Ni content at the surface than the bulk.

Reaction pathways upon oxidation (re-conversion). Figure 6a presents the XANES data upon oxidation of the Li₂O + Ni nanocomposite formed in the *operando* NiO-B cell. Changes in the electronic structure are indicated by the changes in the edge shape and the increasing white-line at 8350 eV. The inset in 6a shows the existence of an apparent isosbestic point, suggesting the presence of only two phases. In principle, this observation is consistent with a mechanism of oxidation of Ni back to NiO. However, the performed PCA indicated the presence of 3 phases (Figures 1 and S2). In comparison to the reduction reaction, the observed changes in edge shape and at the white-line were smaller, suggesting an incomplete re-conversion to NiO.

Relatively small changes were observed in the Ni-oxidation state up to 2.1 V, where about 1 mol of electrons were already transferred (see second dashed line in figure 1), which amounts to a total of 1/3 of the total charge transferred during the reduction reaction. The minor changes in the XAS spectra indicates, that the electrochemical reactions at these potentials are heavily non-transition metal centered, as proposed recently¹⁴, but take place at the layers formed during electrolyte reduction. This conclusion is in agreement with the evolution of the Li K edge spectra above. PCA of the data also revealed the advent of ITFA C, not NiO, spectral features during this electrochemical process. It was only during the small plateau at approximately 2.1 V that re-formation of NiO was observed (Figure 1). Thus, the reaction pathways upon reduction and oxidation were different. Concurrently, the model used to fit the EXAFS data had to be adapted, because the data could not be satisfactorily described by a combination of NiO and metallic Ni. Here, a simple approach of 1 or 2 Ni shells and an additional O shell was taken, where the coordination numbers for oxygen and nickel were fitted. Fourier transform magnitude of k^3 weighted Ni K-edge EXAFS spectra acquired during the oxidation reaction (solid lines) with corresponding fits (dashed lines) are displayed in Figure 6b, and the resulting fit parameters are included in Table 1. During oxidation, the metallic Ni-Ni interaction dominated the radial distribution functions. However, a small contribution from an additional shell at very short distances emerged as Ni was transformed into ITFA C. Contributions from Ni-O and Ni-Ni shells in NiO were again only detected at voltages above 2.1 V. As upon reduction, CN remained low, indicating a large disorder in the sample. Similar mechanistic observations were made during a second conversion cycle, although the results were less conclusive due to the chemical irreversibility of the conversion reaction. The data are thus presented and discussed as Supplementary Information.

Contrasting these results with data collected *ex-situ* from NiO-NP at selected points of conversion/reconversion provided clues into: i) the validity of the pathway found in NiO-B irrespective of initial size,



Table 1 | Parameters of the EXAFS fitting for selected scans of *operando* measurements, ITFAs and NiO-NP (*ex-situ*) at selected states of charge. Values in squared brackets are fixed values, values in brackets are theoretical values. For the fully oxidized *operando* sample two Ni-O shells with the same parameters were fitted. *marks physically unreasonable apparent coordination

sample	Ni metal Fraction	Ni-O shell NiO		Ni-Ni shell metallic		Ni-Ni shell oxide		S_0^2	Reduced χ^2
		CN (6)	dR (R = 2.0890)	CN (12)	dR (R = 2.4917)	CN (12)	dR (R = 2.9543)		
ITFA A	1			6.05	-0.04523			[0.97]	119.7
ITFA B	0	5.55	-0.01876			14.56	0.00147	[0.97]	58.3
ITFA C	0.62	5.010	-0.17257	6.23	-0.03007			[0.97]	600.2
0.0 e⁻ (NiO-B)	0	[6]	0.0073			[12]	0.0024	0.967	51.3
0.5e⁻	0.07	4.95	-0.01899	9.94	-0.03491	9.90	-0.00609	[0.97]	17.3
1.0e⁻	0.34	5.95	-0.00311	11.05	-0.05620	12.35	0.00226	[0.97]	22.2
1.5e⁻	0.46	5.68	0.00857	11.86	-0.05717	10.17	0.00611	[0.97]	79.4
2.0e⁻	0.65	5.35	0.01344	9.88	-0.04001	8.17	0.015405	[0.97]	55.7
2.5e⁻	0.80	33.25*	0.12363	6.71	-0.05556	6.99	-0.00136	[0.97]	64.6
3.0e⁻ (reduced 0V)	0.85	4.190	0.04478	8.39	-0.05507	12.91	-0.02962	[0.97]	73.2
4.0e⁻	0.92	[6]	-0.18912	6.66	-0.03061			[0.97]	134.7
4.5e⁻	0.72	4.50	-0.15923	6.95	-0.02779			[0.97]	47.7
4.7e⁻ (oxidized), 2 Ni-O shells fitted	0.68	3.61	-0.0732930	6.96	-0.01400	4.46	0.20176	[0.97]	27.5
NiO-NP	0.001	6.30	-0.01472	[12]	0.01225	11.66	0.00425	[0.97]	123.
NiO-NP 0 V	1.0	-4.54 *	-0.49938	6.60	-0.00939	-16.40 *	0.24467	[0.97]	93.2
NiO-NP 1.75 V	0.95	2.82	-0.22248	7.11	-0.02118	[12]	0.10975	[0.97]	268.1
NiO-NP 3 V	0.02	14.80*	-0.04120			8.68	-0.00342	[0.97]	313.3

and ii) the possibility of enhancing the efficiency of the reconversion. The main electrochemical signatures of the NiO-NP electrodes in conventional coin cells were similar to NiO-B (Figure S1 in the Supplementary Information). The initial reduction process at 0.8 V was more pronounced in NiO-NP, and an additional broad signature centered at 1.4 V was observed upon oxidation, suggesting possible differences in reaction mechanism. Furthermore, the coulombic efficiency was higher for NiO-NP than NiO-B. When compared to NiO-B, pristine NiO-NP showed very similar XAS features (Figure 7a) and the EXAFS spectra (Figure 7b) contained peaks from higher shells, albeit slightly weakened and distorted. These features are indicative of a high degree of crystallinity and structural coherence despite the primary domains being less than 10 nm in size³¹. After full reduction, the peaks from higher shells vanished and formation of Ni was observed, as also manifested in the edge shift to 8333 eV (XANES). Upon oxidation by recharging the NiO-NP/Li cell to 1.75 V, the XANES signal remained similar to that of metallic Ni, indicating the new process at 1.4 V did not involve significant charge transfer at the transition metal. The EXAFS data showed a contribution at shorter distances than that of Ni-Ni, reminiscent of ITFA C observed in NiO-B. Attempts to fit the data using ITFA A

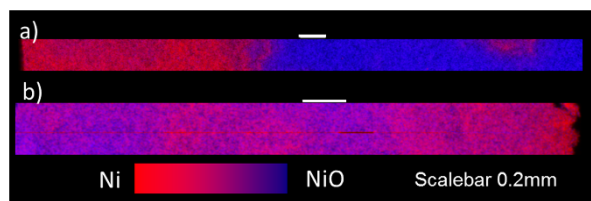


Figure 5 | Maps collected by energy dispersive mapping at the Ni-K edge (*ex-situ*) using total fluorescence yield for NiO-B electrodes reduced by 50% in a Li metal coin cell, at (a) 1C and (b) C/20 rate. The electrodes, which were flat disks, were mounted normal to the observer axis, so that the side facing the bulk of the electrolyte (ion supply) was on top, i.e., represented in the map. The current collector (electron supply) was on the opposite end, away from the observer. The sample depth probed by the fluorescence signal is 4–5 times smaller than the thickness of the electrode. Thus, only the top portion of the electrode was evaluated. Scalebar 0.2 mm.

(Ni) and ITFA C in NiO-B were unsuccessful, suggesting that the exact nature of the intermediate state may be dependent on the microstructure of the initial material. After oxidation to 3 V, the features corresponding to NiO became much more prominent than

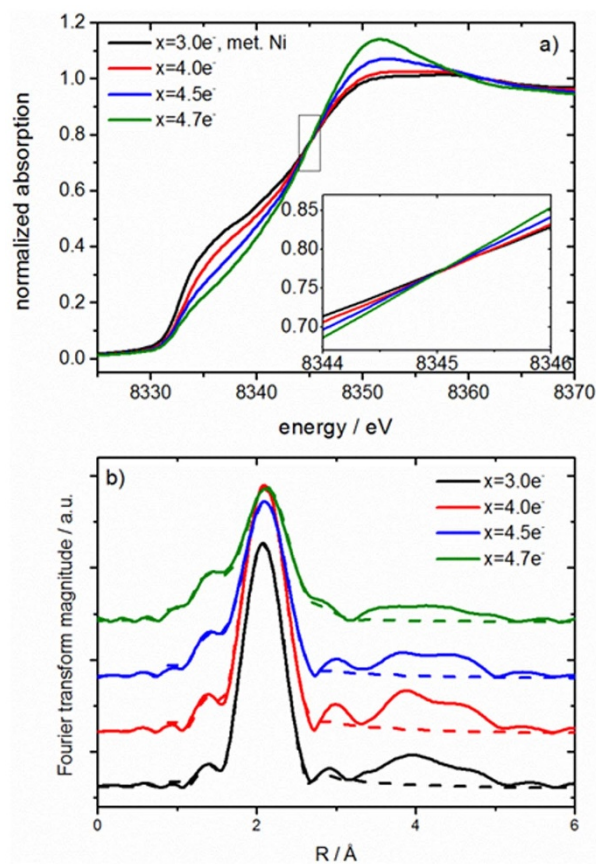


Figure 6 | (a) XANES and (b) Fourier transform magnitude of k^3 weighted Ni-K-edge EXAFS spectra (solid line) and the corresponding fit (dashed line) of selected points of charge during *operando* measurements of NiO-B.

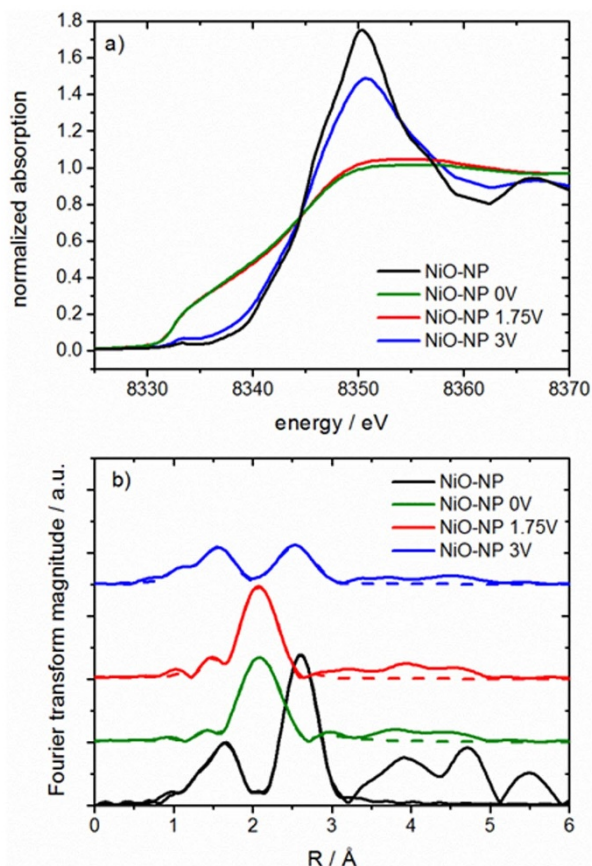


Figure 7 | (a) XANES and (b) EXAFS of NiO-NP at different points of the electrochemical conversion reaction collected *ex-situ*.

in NiO-B, in agreement with the higher coulombic efficiency in the cell. Thus, the overall reaction was definitely more complete in NiO-NP than NiO-B. It is safe to conclude that the length of the 2.1 V plateau is a good indication of the true reversibility of the conversion reaction. Nonetheless, slight differences in the pre-edge and intensity of the white line, as well as dampened features in the post edge could be observed when comparing to pristine NiO. In turn, the Fourier transformed magnitude of the EXAFS spectra revealed a reduced coordination and a significant difference in the relative scattering intensities of the Ni-Ni and Ni-O shells. These effects strongly suggest that the oxide resulting from cycling was still highly defective in nature despite the initial material being formed of very small domains.

Identity of the reaction intermediate. The magnitudes of the Fourier transform for the three ITFAs are shown in Figure 8. ITFA A showed a single main peak at a distance of 2.45 Å, which is in good agreement with the nanoscale Ni formed at 0 V (Table 1). In turn, the O-shell at 2.073 Å and a Ni-shell at 2.95 Å in ITFA B matched the distances of NiO. Finally, ITFA C presented a Ni-Ni interaction at 2.46 Å, similar to Ni, and a shell composed, based on the weak scattering and close distance, of light elements at a distance of about 1.9 Å. The fit of the imaginary part of the data is shown in Figure 8 as well, and reveals good agreement in phase and amplitude. The lack of signals at longer distances limited the determination of bond length and apparent coordination to the first two shells. In contrast to oxygen, nitrogen or carbon can be found at very short first shell distances in the interstitial sites of the Ni metal lattice, leading to small changes in the Ni-Ni distance^{32,33}. Fits using the structures of Ni₃N (ICSD# 280710)³² or Ni₃C (ICSD# 17005)³³ were performed, but were large in error or showed dubious

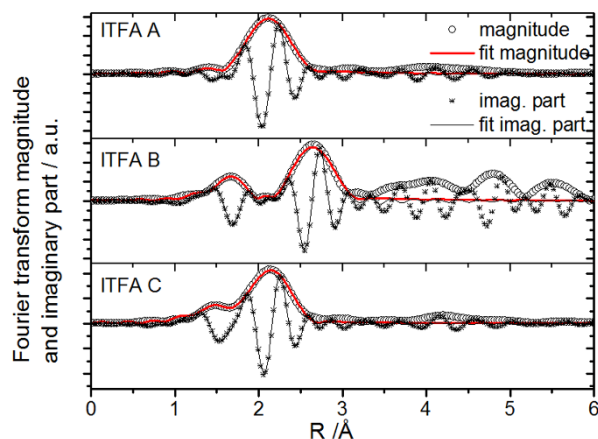


Figure 8 | Fourier transform magnitude of k^3 weighted Ni K-edge EXAFS spectra of the components extracted from PCA (open symbol) and corresponding fit (red line). The full symbols and thinner lines show the corresponding imaginary parts and their fits.

parameters. In a recent report, Moreau *et al.* found significant amounts of P doped on Ni sites in the fcc metallic lattice using EXAFS³⁰, but the resulting distances were significantly above 2.0 Å. Given the large amounts of Li₂O around the Ni clusters in this electrochemical system, it is possible that the scattering is caused by oxygen.

Compounds with similarly short Ni-O distances, such as Ni(OH)₂, NiOOH, or Li_xNi_(1-x)O have generally a much longer Ni-Ni distance (2.9 Å) than the one determined in our measurements (2.46 Å)^{34,35}. However, remarkable similarities were found with experimental analysis of O chemisorption on Ni^{36,37}. It revealed that oxygen can form well defined surface structures on the metal facets. A Ni-O distance of approximately 1.9 Å was determined, yet the lattice parameter of Ni was found to remain almost constant. Attempts to extract structural parameters such as CN from the EXAFS data of ITFA C did not produce reliable results. In contrast, the XANES spectrum of Ni nanoparticles with converted surfaces in one such previous study³⁷ shows similar features to ITFA C in Figure 2b. These observations lead to the conclusion that an intermediate Ni-O phase could be formed during the electrochemical oxidation of the Ni clusters embedded in Li₂O before defective NiO emerged. This pathway also has precedent in the chemisorption studies, where formation of bulk NiO was observed upon extended oxygen exposure³⁶. Since PCA indicated almost complete transformation of Ni to the intermediate (Figure 1), this reaction cannot be limited to the interface between the metal and Li₂O.

Discussion

The conclusions of this study are summarized in Figure 9. The initially crystalline NiO converts to small clusters of Ni dispersed in a Li₂O matrix, which are simultaneously covered with layers resulting from electrolyte decomposition. Such layers impose an overpotential to the reduction of some NiO, which can be further aggravated by electrical disconnection due to the mechanical damage imposed by the drastic volume changes during the phase transformation. As a result, while the secondary reaction is prevalent in the tail end of the electrochemical curve (Figure 2), a small fraction of current is still invested in reducing remnants of the oxide. Electrochemical lithium extraction is enabled by oxygen migration into the Ni lattice to form an intermediate Ni-O compound. With additional driving force for lithium removal, at and above 2.1 V, oxygen continues to diffuse within the system, so that saturation is reached, and formation of nanoscale defective NiO takes place. The electrolyte decomposition layers are also electrochemically active between 0 and 2.1 V vs Li⁺/

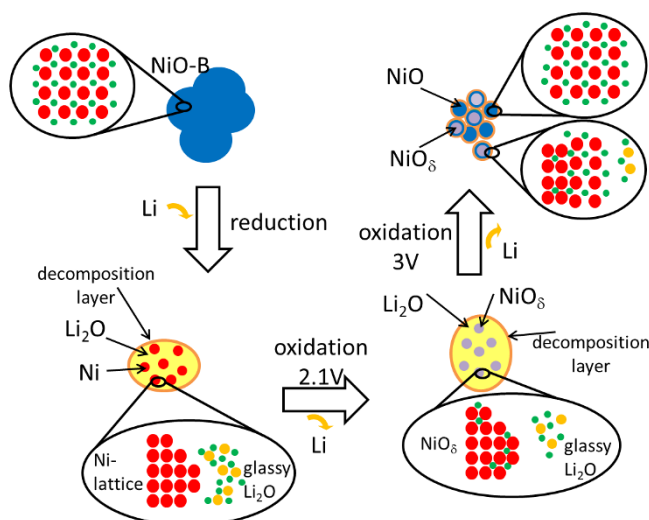


Figure 9 | Schematics of the proposed reaction during the reversible electrochemical conversion of NiO.

Li^0 , in agreement with the observations reported by other for related reactions¹⁴. But these reactions are extremely unlikely to be the reverse of those occurring during reduction. Their electrochemical activity can even impose a change in reaction pathway of the bulk of the electrode³⁸. It is expected that Ni, especially in the form of nanoparticles, has a catalytic role in all these decomposition reactions¹¹. The inherently different chemical pathways for both NiO and the electrolyte, and the fact that oxide crystallinity, and, thus, full atomic ordering, is not recovered constitute sources of voltage hysteresis, which is the ultimate expression of all the contributions to the energy of the system. The hysteresis, while still very large compared to intercalation reactions, was reduced from ~ 1.4 to ~ 0.7 V in the second cycle (Figure S6 in the Supplementary Information). XAS data collected during the second oxidation and reduction reactions, while not completely conclusive due to the mixture of phases existing after the first oxidation, supported the notion that the chemical mechanism is preserved and continues to be asymmetric. Thus, the reduction in hysteresis can be ascribed to microstructural/mechanical energy effects, associated with the change from crystalline to defective NiO as the phase participating in the reaction^{10,39}. The reader is referred to the Supplementary Information for extensive discussion of these points.

The exact nature of the new intermediate observed in the study, especially during oxidation, was not fully established, but incorporation of oxygen into the Ni lattice was found to be the most plausible scenario. Although solubility of oxygen in bulk Ni under equilibrium conditions is known to be low (*ca.* 0.05 at%)⁴⁰ and activation energies for interstitial O diffusion in the metallic framework calculated to be high (1.25–1.54 eV)⁴¹, deviations from thermodynamic equilibrium due to strain and enhanced surface reactivity are not unprecedented in metallic nanoparticles^{42,43}. Oxygen oversaturation in small (2–4 nm) metal clusters was found in Fe-based strengthened steels⁴⁴. The cluster sizes are similar to the metal formed after electrochemical conversion^{45,46}. The driving force for oversaturation was predicted to be the existence of defects in the metallic lattice which showed high affinity toward oxygen, but not other common elements in steel such as C⁴⁷. The differences between the spectra of metallic Ni obtained after reduction of NiO and Ni foil could be indicative of the existence of similar defects in this system, as proposed by others for related systems²⁷. Deviations from the equilibrium metal-oxygen bulk phase diagrams are also well known in surface science. An example is the observation of a metastable epitaxial subsurface oxide in Pd(111) single crystals upon exposure to O_2 ⁴⁸. Formation of this metastable

oxide was hypothesized to be driven by the penalty imposed by the atomic rearrangement involved in the transition from Pd to PdO, the stable oxide, which, just as in our study, eventually formed by saturation upon sustained exposure and increased driving force. Small nanoparticles have such a large surface-to-bulk ratio that a “subsurface oxide” mechanism could be envisioned during lithium extraction from $\text{Li}_2\text{O} + \text{Ni}$ and lead to the complete transformation of the Ni particles into a metastable NiO_δ ($\delta < 1$) state, especially considering that this mechanism is predicted to be favored in late transition metals (and Pd and Ni belong to the same group in the Periodic Table)⁴⁹. Unfortunately, efforts to estimate the oxygen content, δ , by fitting the EXAFS data were not conclusive. Interestingly, the metastable Pd-O intermediate was not observed during the subsequent reduction of PdO, which proceeded straight to Pd metal, resulting in hysteresis. The lack of intermediate during reduction was explained by the different epitaxial pathways involved depending on the starting point. It is possible that similar mechanisms operate in electrochemical conversion reactions.

Our observations provide robust experimental evidence of the consequences of bottlenecks imposed by the diffusion of multiple ionic species as well as electrons during electrochemical conversions^{10,15}. Sauvage *et al.* noted a dramatic increase in conductivity in thin films during the reaction, which was assigned to electronic effects due to Ni domain percolation⁵⁰. Such enhancement provides a large driving force for the reaction to continue in the vicinity of converted domains, especially if the currents imposed are high. Such mechanism is likely behind the large micron-scale inhomogeneities observed in partially reduced electrodes. On charge, it is possible that the formation of the NiO_δ intermediate is also favored by its predictably higher electronic conductivity compared to NiO. In a sense, this observation bears resemblance with the formation of intermediate, high electronic conductivity Magnéli phases (e.g., Ti_5O_9) during the high temperature electro-reduction of TiO_2 ^{51,52}. These phases are crystallographically related to the initial compound and can thus be formed without much rearrangement, leading to an enhancement in conductivity that enables the formation of the metal.

Conclusions

In-depth insight into the mechanism of electrochemical conversion of NiO by Li has been obtained at different scales, from atomic to electrode level. The simplicity of the system renders it a good model for the general class of reactions. First, and most importantly, the voltage hysteresis upon reaction reversal stems, to a large extent, from differences in pathways of reduction and oxidation, imposed by the diffusion of multiple species. While the reduction of NiO proceeds mostly directly to very small, defective Ni nanoparticles and Li_2O , a metastable NiO_δ intermediate is formed upon reoxidation, which preserves the metallic structure. The formation of this intermediate is enabled precisely by the very small size of the Ni clusters, and it is surely at the origin of the reversibility of conversion reactions. The NiO formed at the end of the process was found to be defective as well. Second, inefficiencies in the transformation were created by the concomitant activity of the electrolyte and its degradation products, turning coulometry into an unsuitable tool to determine the amount of material cycled in the electrode. Third, we found that the significant differences in transport between phases creates a driving force toward formation of microscale compositional inhomogeneities. These three observations stress the tremendous challenges toward turning electrochemical conversions into a practical concept of energy storage. While researchers possess tools to alleviate electrolyte reactivity⁵³, overcoming hysteresis would necessarily involve a control over chemical transport not possible today. In addition, the generation of micron-scale inhomogeneities during cycling bears important implications in the design of batteries, as they can lead to overdischarge reactions that compromise safety and durability.



Beyond batteries, this report adds to the existing knowledge of size-dependent compositional metastabilities in materials. While reductions in miscibility gap were known in Li intercalation systems such as LiFePO_4 ⁵⁴, it is now shown they could also exist in simple transition metal systems such as Ni-O. When extremely small crystal sizes are involved, changes in the relative energetics of different phases with respect to the bulk can occur⁵⁵, rendering equilibrium phase diagrams incomplete. These phenomena cut across fields beyond energy storage, such as catalysis and metallurgy. Electrochemistry offers a way of rapidly exploring metastable phase spaces in a variety of conditions⁵⁶.

Methods

Two different sources of NiO were used in this study. Bulk NiO (NiO-B) was purchased from Alfa Aesar (99%, catalog number 12359-18), and used without further purification. NiO nanoplates (NiO-NP) were produced by treating an aqueous solution of $\text{NiSO}_4 \cdot \text{H}_2\text{O}$ and NaOH with a 1 : 2 Ni : OH ratio in hydrothermal conditions, at 160 °C for 12 h, then tempering the product for 2 h at 400 °C. The purity of the product was verified using X-ray diffraction (XRD), see Figure S7 in the Supplementary Information. Scanning electron microscopy (SEM) was performed in a JEOL 7500F operated at 1 kV and 20 μA in gentle beam mode. NiO-B was characterized by large primary particle sizes slightly below 1 micron which in turn form secondary particles of multiple tens of microns in size, whereas NiO-NP were composed of porous hexagonal plates of 100–150 nm diameter and 30–50 nm thickness (Figure S8 in the Supplementary Information). A separate, detailed study by TEM revealed that these plates were composed of 2–5 nm highly ordered domains arranged so as to result in a microporous structure³¹. For transmission electron microscopy, crystals were dispersed on an ultra-thin carbon supported grid and studied in an FEI Tecnai F20 microscope operating at 200 kV using electron energy loss spectroscopy (EELS) and high-angle annular dark field (HAADF) imaging in scanning (STEM) mode.

Porous composite electrodes for electrochemical reactions were prepared with 70 wt% NiO, 15 wt% polyvinylidene fluoride (PVDF) as binder and 15 wt% carbon black conductive additive. The components were mixed in N-methylpyrrolidone (NMP) to form a thick slurry that was subsequently cast onto 15 μm Cu foil and dried in vacuum at 80 °C overnight. The resulting films were either punched as circles of 9.5 mm in diameter for cycling in 2032 coin cells or cut in rectangular form for assembly in pouch cell form. *Ex situ* analyses were performed on samples harvested at reaction levels of interest from coin cells. After cycling, the cells were washed carefully in dimethyl carbonate (DMC) and stored in inert atmosphere until the measurement was performed. In turn, pouch cells were encased between two aluminum plates to ensure adequate levels of pressure and used in the *operando* analyses. A 2 × 10 mm (height × width) rectangular hole was drilled in the plates to allow the transmission of the synchrotron beam. In all cases, lithium metal was used as counter and pseudo-reference electrode, with Celgard 2400 impregnated with 1 M LiPF_6 in 45 : 55 EC : DEC electrolyte as separator. The cells were galvanostatically cycled between 0 and 3 V vs. Li^+/Li^0 at C/n rate, defined as the current density required to achieve full theoretical capacity ($C = 718 \text{ mAh/g}$) in n hours. All cell assembly and disassembly was performed under continuously purified Ar atmosphere in a glovebox with levels of $\text{H}_2\text{O} < 0.1 \text{ ppm}$ and $\text{O}_2 < 0.1 \text{ ppm}$. VMP3 and VSP galvanostat/potentiostats (Bio-Logic USA, LLC) were used for the *ex situ* and *operando* measurements, respectively. All electrical potential values discussed in this paper are referred to the Li^+/Li^0 couple ($E^0 = -3.04 \text{ V}$ vs. normal hydrogen electrode).

Bulk X-ray absorption spectroscopy (XAS) data was collected at beamline 4-1 of the Stanford Synchrotron Radiation Lightsource (SSRL) at SLAC National Accelerator Laboratory (Menlo Park, USA) using a Si(220) double crystal monochromator. Spectra were acquired in transmission mode around the Ni-K edge (8333 eV), in the energy range from 8100 to 8950 eV ($k = 12.5$). Higher harmonics in the X-ray beam were minimized by detuning the Si(220) monochromator by 35% at the Ni K-edge. A Ni-metal reference foil between the second and third ionization chamber was used for energy calibration.

Micro-XAS experiments were performed at the Ni-K edge (8333 eV) at beamline 10.3.2 of the Advanced Light Source (ALS) at Lawrence Berkeley National Laboratory (Berkeley, USA). Spectra were acquired in total fluorescence yield (TFY) mode and total electron yield (TEY) mode simultaneously to probe different depths. TFY detection was done using a seven-element Ge solid-state (Canberra) detector. High resolution Ni chemical maps were acquired at several incident energies: 8320 (pre-edge background), 8333.8, 8349 and 8388 eV (for normalization) with a spot size of 5 × 5 μm on the sample and 50 ms dwell time/pixel. The values of 8333.8 and 8349 eV were selected to give the highest contrast between Ni^0 and Ni^{2+} (NiO), respectively, as extracted from bulk data for reference samples. The individual energy maps were normalized, dead time corrected and registered to each other to correct for small spatial shifts. Chemical phase maps were compiled from the intensity ratios at the selected energies using methods described in the literature⁵⁷. At selected points on the sample full EXAFS spectra were acquired. Standard procedures for experimental data reduction, Fourier transformed EXAFS and FEFF fits were performed using Athena and Artemis of the IFEFFIT suite⁵⁸. Principal component analysis (PCA) including iterative target-factor analysis was performed using software available at beamline 10.3.2 and its website (<http://www-esg.lbl.gov/uxas>).

XAS at the Li-K-edge (56 eV) was performed at beamline 11ID-2 (VLS PGM endstation)⁵⁹ of the Canadian Light Source (Saskatchewan, Canada) by detecting the total fluorescence yield. Samples were prepared under inert atmosphere, mounted to a metal sample plate using carbon tape under Ar atmosphere in a glove bag attached to the beamline endstation, then transferred into a vacuum chamber under 5×10^{-7} torr or less. Powdered reference samples (Li_2CO_3 , Li_2O , LiOH , and LiF) were pressed into indium foil before mounting. XAS scans were performed across the Li K-edge from high to low X-ray energy with an average scan time of 45 minutes. Samples were aligned with the surface normal parallel to the incident radiation. The illuminating beam spot was on average 0.5 mm × 0.5 mm and scans were repeated on multiple spots to check for beam damage effects. Total fluorescence yield (TFY) spectra were collected using a channel plate detector mounted with a surface normal at a 45° degree angle with respect to the incident X-ray beam. Spectra were normalized to the incident beam current as measured by a nickel mesh upstream from the sample.

- Greeley, J. & Markovic, N. M. The road from animal electricity to green energy: combining experiment and theory in electrocatalysis. *Energy Environ. Sci.* **5**, 9246–9256 (2012).
- Weber, A. Z. *et al.* Redox flow batteries: a review. *J. Appl. Electrochem.* **41**, 1137–1164 (2011).
- Armand, M. & Tarascon, J.-M. Building better batteries. *Nature* **451**, 652–7 (2008).
- Larcher, D. *et al.* Recent findings and prospects in the field of pure metals as negative electrodes for Li-ion batteries. *J. Mater. Chem.* **17**, 3759–3772 (2007).
- Cabana, J., Monconduit, L., Larcher, D. & Palacin, M. R. Beyond intercalation-based Li-ion batteries: the state of the art and challenges of electrode materials reacting through conversion reactions. *Adv. Energy Mater.* **22**, E170–192 (2010).
- Bruce, P. G., Freunberger, S. A., Harwick, L. J. & Tarascon, J.-M. Li–O₂ and Li–S batteries with high energy storage. *Nat. Mater.* **11**, 19–30 (2012).
- Zheng, H., Li, J., Song, X., Liu, G. & Battaglia, V. S. A comprehensive understanding of electrode thickness effects on the electrochemical performances of Li-ion battery cathodes. *Electrochim. Acta* **71**, 258–265 (2012).
- Wang, F. *et al.* Tracking lithium transport and electrochemical reactions in nanoparticles. *Nat. Commun.* **3**, 1201 (2012).
- Hu, Y.-S. *et al.* Electrochemical lithiation synthesis of nanoporous materials with superior catalytic and capacitive activity. *Nat. Mater.* **5**, 713–717 (2006).
- Doe, R. E., Persson, K. A., Meng, Y. S. & Ceder, G. First-Principles Investigation of the Li–Fe–F Phase Diagram and Equilibrium and Nonequilibrium Conversion Reactions of Iron Fluorides with Lithium. *Chem. Mater.* **20**, 5274–5283 (2008).
- Gmitter, A. J. *et al.* Formation, dynamics, and implication of solid electrolyte interphase in high voltage reversible conversion fluoride nanocomposites. *J. Mater. Chem.* **20**, 4149–4161 (2010).
- Laruelle, S. *et al.* On the Origin of the Extra Electrochemical Capacity Displayed by MO/Li Cells at Low Potential. *J. Electrochem. Soc.* **149**, A627–A634 (2002).
- Ponrouch, A., Cabana, J., Dugas, R., Slack, J. L. & Palacin, M. R. Electroanalytical study of the viability of conversion reactions as energy storage mechanisms. *RSC Adv.* **4**, 35988–35996 (2014).
- Lowe, M. A., Gao, J. & Abruña, H. D. In operando X-ray studies of the conversion reaction in Mn_2O_4 lithium battery anodes. *J. Mater. Chem. A* **1**, 2094–2103 (2013).
- Doe, R. E., Persson, K. A., Hautier, G. & Ceder, G. First Principles Study of the Li–Bi–F Phase Diagram and Bismuth Fluoride Conversion Reactions with Lithium. *Electrochem. Solid-State Lett.* **12**, A125–128 (2009).
- Chadwick, A. V. *et al.* Formation and Oxidation of Nanosized Metal Particles by Electrochemical Reaction of Li and Na with NiCo_2O_4 : X-ray Absorption Spectroscopic Study. *J. Phys. Chem. C* **111**, 4636–4642 (2007).
- Choi, H. C. *et al.* Local Structural Characterization for Electrochemical Insertion–Extraction of Lithium into CoO with X-ray Absorption Spectroscopy. *J. Phys. Chem. B* **106**, 9252–9260 (2002).
- Zhong, K. *et al.* Investigation on porous MnO microsphere anode for lithium ion batteries. *J. Power Sources* **196**, 6802–6808 (2011).
- Rieck, H. & Hoppe, R. Ein neues Oxonicoalat: Li_2NiO_2 . *Z. Anorg. Allg. Chem.* **392**, 193–321 (1972).
- Liu, H., Wang, G., Liu, J., Qiao, S. & Ahn, H. Highly ordered mesoporous NiO anode material for lithium ion batteries with an excellent electrochemical performance. *J. Mater. Chem.* **21**, 3046 (2011).
- Rosser, A., Reich, T. & Bernhard, G. Complexation of uranium(VI) with protocatechuic acid-application of iterative transformation factor analysis to EXAFS spectroscopy. *Anal. Bioanal. Chem.* **376**, 631–8 (2003).
- Aurbach, D. Review of selected electrode–solution interactions which determine the performance of Li and Li ion batteries. *J. Power Sources* **89**, 206–218 (2000).
- Ponrouch, A., Taberna, P.-L., Simon, P. & Palacin, M. R. On the origin of the extra capacity at low potential in materials for Li batteries reacting through conversion reaction. *Electrochim. Acta* **61**, 13–18 (2012).
- Henke, B. L., Gullikson, E. M. & Davis, J. C. X-ray interactions: Photoabsorption, scattering, transmission and reflection at $e = 50\text{--}30000 \text{ eV}$, $Z = 1\text{--}92$. *At. Data Nucl. data tables* **54**, 181–342 (1993).
- Anspoks, A., Kuzmin, A., Kalinko, A. & Timoshenko, J. Probing NiO nanocrystals by EXAFS spectroscopy. *Solid State Commun.* **150**, 2270–2274 (2010).



26. Sasaki, S., Fujino, K. & Takeuchi, Y. X-ray Determination of Electron-Density Distributions in Oxides, MgO, MnO, CoO, NiO, and Atomic Scattering Factors of their Constituent Atoms. *Proc. Japan Acad. Ser. B* **55**, 43–48 (1979).
27. Shyam, B. *et al.* Structural and mechanistic revelations on an iron conversion reaction from pair distribution function analysis. *Angew. Chem. Int. Ed. Engl.* **51**, 4852–4855 (2012).
28. Miller, J. T. *et al.* The effect of gold particle size on Au-Au bond length and reactivity toward oxygen in supported catalysts. *J. Catal.* **240**, 222–234 (2006).
29. Calvin, S. *et al.* Determination of crystallite size in a magnetic nanocomposite using extended x-ray absorption fine structure. *J. Appl. Phys.* **94**, 778–783 (2003).
30. Moreau, L. M. *et al.* Unintended phosphorus doping of nickel nanoparticles during synthesis with TOP: a discovery through structural analysis. *Nano Lett.* **12**, 4530–9 (2012).
31. Shukla, A. K., Ercius, P., Gautam, A. R. S., Cabana, J. & Dahmen, U. Electron Tomography Analysis of Reaction Path during Formation of Nanoporous NiO by Solid State Decomposition. *J. Cryst. Growth Des.* **14**, 2453–2459 (2014).
32. Leineweber, A., Jacobs, H. & Hull, S. Ordering of Nitrogen in Nickel Nitride Ni₃N Determined by Neutron Diffraction. *Inorg. Chem.* **40**, 5818–5822 (2001).
33. Nagakura, S. Study of Metallic Carbides by Electron Diffraction Part II. Crystal Structure Analysis of Nickel Carbide. *J. Phys. Soc. Japan* **13**, 1005–1014 (1958).
34. Casas-Cabanas, M., Canales-Vazquez, J., Rodríguez-Carvajal, J. & Palacin, M. R. Deciphering the structural transformations during nickel oxyhydroxide electrode operation. *J. Am. Chem. Soc.* **129**, 5840–2 (2007).
35. Pickering, I. J., George, J. G. N., Lewandowski, J. T. & Jacobson, A. J. Nickel K-Edge X-ray Absorption Fine Structure of Lithium Nickel Oxides. *J. Am. Chem. Soc.* **115**, 4137–4144 (1993).
36. Kortan, A. R. & Park, R. L. Phase diagram of oxygen chemisorbed on nickel (111). *Phys. Rev. B* **23**, 6340–6347 (1981).
37. Lewis, P. H. The effects of oxygen adsorption on the K X-ray absorption edge of alumina supported nickel. *J. Physical Chem.* **64**, 1103–1109 (1960).
38. Gmitter, A. J., Halajko, A., Sideris, P. J., Greenbaum, S. G. & Amatucci, G. G. Subsurface diffusion of oxide electrolyte decomposition products in metal fluoride nanocomposite electrodes. *Electrochim. Acta* **88**, 735–744 (2013).
39. Delmer, O., Balaya, P., Kienle, L. & Maier, J. Enhanced Potential of Amorphous Electrode Materials: Case Study of RuO₂. *Adv. Mater.* **20**, 501–505 (2008).
40. Neumann, J. P., Zhong, T. & Chang, Y. A. The Ni-O (Nickel-Oxygen) System 58.69 15.9994. *Bull. Alloy Phase Diagrams* **5**, 141–144 (1984).
41. Megchiche, E. H., Amarouche, M. & Mijoule, C. First-principles calculations of the diffusion of atomic oxygen in nickel: thermal expansion contribution. *J. Phys. Condens. Matter* **19**, 296201 (2007).
42. Zhang, H., Gilbert, B., Huang, F. & Banfield, J. F. Water-driven structure transformation in nanoparticles at room temperature. *Nature* **424**, 1025–1029 (2003).
43. Gilbert, B., Huang, F., Zhang, H., Waychunas, G. & Banfield, J. F. Nanoparticles: strained and stiff. *Science* **305**, 651–4 (2004).
44. Larson, D. J., Maziasz, P. J., Kim, I. & Miyahara, K. Three-dimensional atom probe observation of nanoscale titanium-oxygen clustering in an oxide-dispersion-strengthened Fe-12Cr-3W-0.4Ti + Y₂O₃ ferritic alloy. *Scr. Mater.* **44**, 359–364 (2001).
45. Wang, F. *et al.* Conversion reaction mechanisms in lithium ion batteries: study of the binary metal fluoride electrodes. *J. Am. Chem. Soc.* **133**, 18828–18836 (2011).
46. Poizot, P., Laruelle, S., Grubeon, S., Dupont, L. & Tarascon, J. M. Nano-sized transition-metal oxides as negative-electrode materials for lithium-ion batteries. *Nature* **407**, 496–9 (2000).
47. Fu, C., Krčmar, M., Painter, G. & Chen, X.-Q. Vacancy Mechanism of High Oxygen Solubility and Nucleation of Stable Oxygen-Enriched Clusters in Fe. *Phys. Rev. Lett.* **99**, 225502 (2007).
48. Ketteler, G. *et al.* In situ spectroscopic study of the oxidation and reduction of Pd(111). *J. Am. Chem. Soc.* **127**, 18269–73 (2005).
49. Gustafson, J. *et al.* Self-Limited Growth of a Thin Oxide Layer on Rh(111). *Phys. Rev. Lett.* **92**, 126102 (2004).
50. Sauvage, F., Tarascon, J., Baudrin, E. & Verne, D. P. J. In Situ Measurements of Li Ion Battery Electrode Material Conductivity: Application to Li_xCoO₂ and Conversion Reactions. *J. Phys. Chem. C* **111**, 9624–9630 (2007).
51. Chen, G. G. Z., Fray, D. J. D. & Farthing, T. W. T. Direct electrochemical reduction of titanium dioxide to titanium in molten calcium chloride. *Nature* **407**, 361–364 (2000).
52. Styles, M. J. *et al.* A furnace and environmental cell for the in situ investigation of molten salt electrolysis using high-energy X-ray diffraction. *J. Synchrotron Radiat.* **19**, 39–47 (2012).
53. Etacheri, V., Marom, R., Elazari, R., Slitra, G. & Aurbach, D. Challenges in the development of advanced Li-ion batteries: a review. *Energy Environ. Sci.* **4**, 3243–3262 (2011).
54. Yamada, A. *et al.* Room-temperature miscibility gap in Li_xFePO₄. *Nat. Mater.* **5**, 357–60 (2006).
55. Navrotsky, A., Ma, C., Lilova, K. & Birkner, N. Nanophase transition metal oxides show large thermodynamically driven shifts in oxidation-reduction equilibria. *Science* **330**, 199–201 (2010).
56. Guignard, M. *et al.* P2-Na_xVO₂ system as electrodes for batteries and electron-correlated materials. *Nat. Mater.* **12**, 74–80 (2013).
57. Marcus, M. A. X-ray photon-in/photon-out methods for chemical imaging. *TRAC-TRENDS Anal. Chem.* **29**, 508–517 (2010).
58. Newville, M. *et al.* Analysis of multiple-scattering XAFS data using theoretical standards. *Phys. B* **208 & 209**, 154–156 (1995).
59. Hu, Y. F., Zuiin, L., Reining, R. & Sham, T. K. VLS-PGM Beamline at the Canadian Light Source. *AIP Conf. Proc.* **879**, 535–538 (2007).

Acknowledgments

This work was primarily supported by the Assistant Secretary for Energy Efficiency and Renewable Energy, Office of Vehicle Technologies of the U.S. Department of Energy (DOE) under Contract No. DE-AC02-05CH11231, as part of the Batteries for Advanced Transportation Technologies (BATT) Program. Exceptions to this statement are as follows. TY was supported as part of the Joint Center for Energy Storage Research, an Energy Innovation Hub funded by the U.S. DOE, Office of Science, Basic Energy Sciences. EM and AM wish to acknowledge funding from the Natural Sciences and Engineering Research Council (NSERC) and the Canada Research Chair program. P.F. Teh grateful acknowledges the World Future Foundation (WFF) for PhD Prize in Environmental and Sustainability Research@NTU 2014. The μ -XAS work was conducted at the Advanced Light source which is supported by the Director, Office of Science, Office of Basic Energy Sciences, of the U.S. DOE under Contract No. DE-AC02-05CH11231. The *operando* XAS experiments were carried out at the Stanford Synchrotron Radiation Lightsource, a Directorate of SLAC National Accelerator Laboratory and an Office of Science User Facility operated for the U.S. DOE Office of Science by Stanford University. The SSRL Structural Molecular Biology Program is supported by the DOE Office of Biological and Environmental Research, and by the National Institutes of Health, National Institute of General Medical Sciences (including P41GM103393) and the National Center for Research Resources (P41RR001209). Supporting *ex situ* XAS was carried out at the Pacific Northwest Consortium-X-ray Science Division (PNC/XSD) facilities at the Advanced Photon Source (APS), supported by the U.S. DOE Office of Science, the Canadian Light Source (CLS) and its funding partners, the University of Washington, and the APS. Use of the APS, an Office of Science User Facility operated for the DOE by Argonne National Laboratory, was supported by Contract No. DE-AC02-06CH11357. The Li K edge XAS described in this paper was performed in parts at the CLS, which is supported by the NSERC of Canada, the National Research Council Canada, the Canadian Institutes of Health Research, the Province of Saskatchewan, Western Economic Diversification Canada, and the University of Saskatchewan. The authors further acknowledge support of the National Center for Electron Microscopy, Lawrence Berkeley National Laboratory, which is supported by the U.S. Department of Energy under Contract DE-AC02-05CH11231. The authors wish to thank Prof. Scott Calvin (Sarah Lawrence College, NY) and Dr. Mahalingam Balasubramanian (APS), as well as the beamline staff at SSRL, APS and CLS for their help and support during the experiments. The contents of this publication are solely the responsibility of the authors and do not necessarily represent the official views of NIGMS, NCRN or NIH.

Author contributions

U.B., M.A.M., T.Y. and J.C. collected the Ni-K edge XAS data. U.B. and M.A.M. analyzed the EXAFS data. A.K.S. performed the TEM and EELS measurements. The samples were prepared, electrochemically cycled by P.F.T. and U.B., supervised by M.S. and J.C.. The Li-XAS experiments were performed by E.M. and A.M. U.B. and J.C. wrote the manuscript. All authors reviewed the manuscript.

Additional information

Supplementary information accompanies this paper at <http://www.nature.com/scientificreports>

Competing financial interests: The authors declare no competing financial interests.

How to cite this article: Boesenberg, U. *et al.* Asymmetric pathways in the electrochemical conversion reaction of NiO as battery electrode with high storage capacity. *Sci. Rep.* **4**, 7133; DOI:10.1038/srep07133 (2014).



This work is licensed under a Creative Commons Attribution-NonCommercial-ShareAlike 4.0 International License. The images or other third party material in this article are included in the article's Creative Commons license, unless indicated otherwise in the credit line; if the material is not included under the Creative Commons license, users will need to obtain permission from the license holder in order to reproduce the material. To view a copy of this license, visit <http://creativecommons.org/licenses/by-nc-sa/4.0/>